Land Surface Temperature Retrieval Based on Thermal Infrared Channel Decomposed Split-Window Algorithm

Xin Ye, Huazhong Ren, Jinshun Zhu, Hui Zeng, Baozhen Wang, He Huang, and Wenjie Fan

***Abstract*—Land surface temperature (LST) is an important parameter affecting ground-air energy exchange, and can be applied in many fields such as drought monitoring, evapotranspiration estimation, and crop yield assessment. The single-channel (SC) algorithm only needs thermal infrared (TIR) data with only one channel to retrieve the LST, but requires accurate atmospheric correction, which is difficult to guarantee in many cases. The split-window (SW) algorithm exploits the difference in atmospheric absorption of adjacent channels and can accurately obtain the LST without atmospheric parameters, but the input requirement of two TIR channels makes the application limited. Some previous studies found that there is a strong correlation between the top-of-atmosphere thermal radiance in adjacient TIR channels with similar wavelength ranges, which makes it possible to decompose a single TIR channel into two TIR channels with close wavelengths using empirical relationships with errors smaller than those caused by the uncertainty of atmospheric correction. In this article, Landsat-7 ETM+ TIR data was decomposed into two virtual TIR channels by fusing with the simultaneously observed Terra moderate resolution imaging spectroradiometer (MODIS) data, and the channel decomposed SW (TCD-SW) based on the generalized nonlinear SW algorithm was developed and applied to retrieve the LST to eliminate the dependence on atmospheric parameters. The validation results using the simulation dataset, ground-measured site data, and well-validated MODIS sea surface temperature product showed that the proposed TCD-SW algorithm achieved more accurate results than the SC algorithm, being more advantageous in the humid atmosphere. The TCD-SW algorithm can be used as a potential new method for LST retrieval from remote sensing data with only one TIR channel under complex atmospheric conditions.**

***Index Terms*—Atmospheric correction, land surface temperature (LST), single-channel (SC) algorithm, split-window (SW) algorithm, thermal radiance transfer.**

Manuscript received April 18, 2022; revised May 23, 2022; accepted June 5, 2022. Date of publication June 10, 2022; date of current version June 27, 2022. This work was supported in part by the National High-Resolution Earth Observation Project of China under Grant 04-H30G01-9001-20/22, in part by the China Postdoctoral Science Foundation under Grant 2021M690199, in part by the National Natural Science Foundation of China under Grant 42101340, and in part by the National Civil Aerospace Project of China under Grant D040102. *(Corresponding author: Huazhong Ren.)*

Xin Ye, Jinshun Zhu, Hui Zeng, Baozhen Wang, and Wenjie Fan are with the Institute of Remote Sensing and Geographic Information System, School of Earth and Space Sciences, Peking University, Beijing 100871, China, and also with the Beijing Key Laboratory of Spatial Information Integration and Its Application, Peking University, Beijing 100871, China (e-mail: xinye@pku.edu.cn; zhujinshun@pku.edu.cn; zenghui@pku.edu.cn; baozhen3617@stu.pku.edu.cn; fanwj@pku.edu.cn).

Huazhong Ren is with the Institute of Remote Sensing and Geographic Information System, School of Earth and Space Sciences, Peking University, Beijing 100871, China, and with the Beijing Key Laboratory of Spatial Information Integration and Its Application, Peking University, Beijing 100871, China, and also with the University Joint Remote Sensing Application Research Center, Beijing 100871, China (e-mail: renhuazhong@pku.edu.cn).

He Huang is with the Chongqing Planning Exhibition Gallery, Chongqing Planning Research Institute, Chongqing 400061, China (e-mail: hh_cqprc@163.com).

Digital Object Identifier 10.1109/JSTARS.2022.3181505

I. Introduction

LAND surface temperature (LST) is a key factor in characterizing the exchange of energy between the land surface and the atmosphere and has been widely used in a variety of fields such as climate change, agriculture, and environmental protection. Thermal infrared (TIR) remote sensing technology can observe long time series and large spatial scales of land surface thermal radiance, which has obvious advantages in spatial continuity, wide coverage, and acquisition efficiency compared with the traditional ground-measured method. The study of retrieving LST from the TIR remote sensing image started in the 1970s [1] and has attracted much attention [2]. Several methods have been proposed based on different TIR sensors over the decades, typical of which are the single-channel (SC) algorithm [3]–[6] and the split-window (SW) algorithm [7]–[11].

The SC algorithm assumes that the land surface emissivity (LSE) and atmospheric profiles or near-surface air temperature, water vapor content, and other parameters that can be used for atmospheric correction are known [3]–[6], then the LST can be retrieved by inverting the radiative transfer equation (RTE). It is currently the only LST retrieval method for the TIR remote sensing sensors with one channel within the atmospheric window, such as Landsat 5 TM and Landsat-7 ETM+ data. However, the LST retrieval accuracy of the SC algorithm is directly influenced by the uncertainty of the atmospheric profile and the atmospheric correction results using empirical relations may be poor for humid atmospheres [2], [3]. For the SW algorithm, the LST is calculated by a linear or nonlinear combination of the brightness temperature (BT) at the top of the atmosphere using the difference in atmospheric absorption between adjacent TIR channels [7], [11], [12]. Compared to the SC algorithm, the SW algorithm requires only the LSE and not the atmospheric information, which reduces one of the possible causes of error and achieves better performances of LST retrieval than the SC algorithm according to the previous studies [13], [14]. Since more than two channels of BTs are needed [8], [9], [15], the SW algorithm cannot be used for sensors with only one TIR channel, so its application is not as wide as that of the SC algorithm.

A strong correlation was found between the top-of-atmosphere (TOA) channel thermal radiance at similar wavelength ranges in some studies of TIR data simulation and in-orbit cross recalibration [9], [16]–[18], also including moderate resolution imaging spectroradiometer (MODIS) and Landsat data [19], which can be fitted with linear regression without introducing large errors. Therefore, it can be used to decompose a single TIR channel into two adjacent channels if the correlation is both satisfied for the original channel and the two decomposed channels. Subsequently, the SW algorithm can be developed using the decomposed TIR channels to eliminate atmospheric effects to optimize the LST retrieval results due to atmospheric uncertainties in the SC algorithm. According to the above analysis, this article first demonstrated the correlation between the TOA radiance of Landsat-7 channel 6 and MODIS channels 31 and 32 using the simulation dataset under various atmospheric and land surface conditions, then propose a linear model to decompose the Landsat-7 TIR channel into two virtual MODIS TIR channels considering the characteristics of these two remote sensing data sources, and a new SW algorithm was developed and validated for the two decomposed Landsat-7 TIR channels. This article is organized as follows: Section II describes the development of the TIR channel decomposed SW (TCD-SW) algorithm, Section III provides the theoretical accuracy based on the simulation dataset, and Section IV gives the LST retrieval application and validation results of real Landsat-7 remote sensing images, and Section V presents the discussions and conclusions.

II. Development of the LST Retrieval Algorithm

According to the RTE, the thermal radiance observed by the satellite at the top of the atmosphere can be expressed as

$$L_{\mathrm{TOA}} = [\varepsilon \cdot B(T_S) + (1-\varepsilon) \cdot L_{A\downarrow}] \cdot \tau + L_{A\uparrow} \qquad (1)$$

where τ is the atmosphere upward transmittance, $L_{A\uparrow}$ is the atmosphere upward radiance, $L_{A\downarrow}$ is the atmosphere downward radiance, ε is the channel emissivity, and $B(T_S)$ is the channel blackbody radiance when the LST is T_S. It is important to note that the parameters in the RTE are obtained by integrating with the spectral response function (SRF) and are related to the remote sensing data channels. Therefore, this article proposes the TCD-SW algorithm by assuming that for different TIR data sources with similar channel settings, the observed TOA radiance should be strongly correlated under the same land surface and atmospheric conditions.

Fig. 1 shows the flowchart of the development of the TCD-SW algorithm. First, the atmospheric parameters ($L_{A\downarrow}, L_{A\uparrow}, \tau$) were obtained using the moderate-spectral-resolution atmospheric transmittance (MODTRAN) model and the thermodynamic initial guess retrieval (TIGR) version three atmospheric profiles [20]. Second, several typical LSE samples were selected from the ASTER and the University of California at Santa Barbara (UCSB) emissivity database [21], [22], and integrated with the SRF of Landsat-7 TIR and MODIS 31 and 32 channels data, which was selected because of the suitability of developing SW algorithms, similar wavelength ranges, and similar satellite observation times, to calculate the channel emissivity. Then the

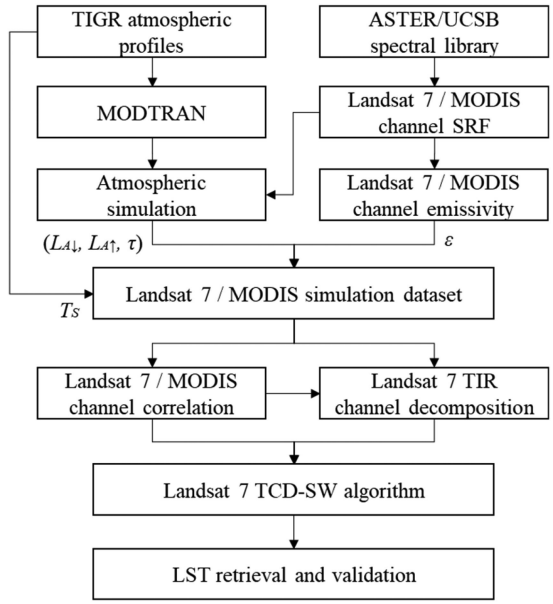

Fig. 1. Flowchart of the proposed TCD-SW algorithm.

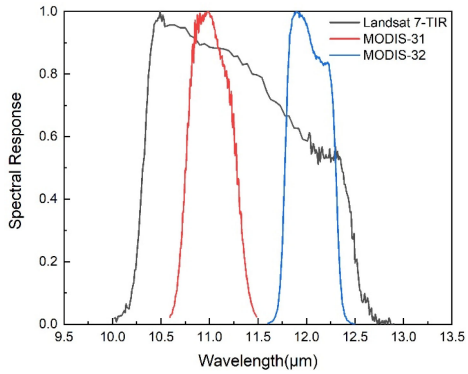

Fig. 2. SRFs of MODIS and Landsat-7 TIR channel.

simulation datasets of TOA thermal radiance under different atmospheric and land surface conditions were generated based on the RTE and used to establish the empirical correlation between the two TIR sensors and to decompose the real Landsat-7 TIR channel into two virtual TIR channels in the same configuration with MODIS 31 and 32 channels (hereinafter referred to as virtual MODIS TIR channels). Finally, the LST was retrieved by the Landsat-7 TCD-SW algorithm which was inspired by the generalized nonlinear SW algorithm used to produce MODIS LST products [11], [23]–[25].

A. Simulation Dataset

As can be seen from the SRFs of Landsat-7 TIR and MODIS 31/32 channels (see Fig. 2), the wavelength range of the Landsat-7 TIR channel covers both MODIS channels. To simulate different atmospheric conditions, 946 clear-sky profiles were selected from the TIGR atmospheric profiles dataset, including polar, mid-latitude, and tropical atmospheric profiles with the column water vapors (CWVs) range in [0.0, 6.3] g/cm^2, and

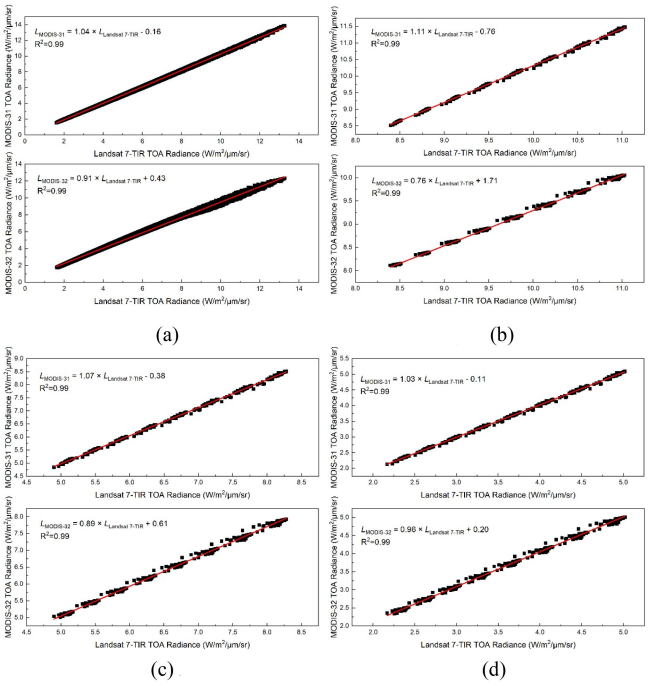

Fig. 3. Empirical relationships between TOA radiance of Landsat-7 and MODIS data under different atmospheric conditions. (a) Overall. (b) Tropical (CWV = 4.35 g/cm^2). (c) Mid-Latitude (CWV = 1.76 g/cm2). (d) Polar (CWV = 0.15 g/cm^2).

drive MODTRAN to obtain three atmospheric parameters (τ, $L_{A\uparrow}$, and $L_{A\downarrow}$). For land surface parameters, the LST (T_S) is the air temperatures at the bottom boundary of TIGR profiles (T_0) plus [−15 K, 20 K] with an interval variation range of 5 K. The channel LSE ε is calculated by integrating the 77 sample spectral selected from the ASTER/UCSB spectral database, including 36 soil samples, 23 rock samples, 14 vegetation samples, and 4 water samples, with the SRFs and calculated by the following equation:

$$\varepsilon = \frac{\int_{\lambda 1}^{\lambda 2} f(\lambda)\,\varepsilon(\lambda)\,d\lambda}{\int_{\lambda 1}^{\lambda 2} f(\lambda)\,d\lambda} \tag{2}$$

where $f(\lambda)$ is the channel SRF and $\varepsilon(\lambda)$ is the emissivity of one sample at wavelength λ. The simulation dataset in this article consists of a total of 582 736 records (946 atmospheric profiles × 77 land surface emissivities × 8 LSTs) of TOA radiance on which the correlation between the TOA radiance of different TIR channels will be analyzed.

B. TIR Channel Decomposition

Based on the simulation dataset, the empirical relationships of TOA thermal radiance fit for Landsat-7 TIR - MODIS 31 channel and Landsat-7 TIR - MODIS 32 channel under different atmospheric conditions were obtained separately. Fig. 3 shows the distribution of the overall atmospheric profiles, one tropical profile with CWV = 4.35 g/cm^2, one mid-latitude profile with CWV = 1.76 g/cm^2, and one polar profile with CWV = 0.15 g/cm^2. As can be seen from the figures, the overall linear fittings have good effects with low residuals and R-squared > 0.99, and the root-mean-square errors (RMSEs) for all records are 0.038 W/m^2/μm/sr and 0.085 W/m^2/μm/sr, respectively. The performance of fitting the MODIS 31 channel is better than that of the MODIS 32 channel, which is related to the distribution of the SRF, as the high response region of the Landsat-7 TIR channel and the MODIS 31 channel overlap more. The TOA radiance data in Fig. 3(b)–(d) all include eight subsets with similar distributions due to the LST in the simulation dataset being set as the air temperature at the bottom boundary of each TIGR profile plus [−15 K, 20 K] with an interval variation range of 5 K. There are some differences in the values of the fitted coefficients for different atmospheric types, which may be mainly due to the effect of water vapor and atmospheric temperature, the atmospheric parameters in Fig. 3(b)–(d), the atmospheric transmittance gradually decreases, while the upward and downward radiance grows. Besides, all R-squared values are also greater than 0.99 and the pattern of the fitted parameters is consistent, with the slope of the fitted results in the MODIS 31 channel (1.11 for the tropical profile, 1.07 for the mid-latitude profile, 1.03 for the polar profile and 1.04 for the overall cases) being greater than that of MODIS 32 channel (0.76 for the tropical profile, 0.89 for the mid-latitude profile, 0.96 for the polar profile and 0.91 for the overall cases), while the intercept of the MODIS 31 channel (-0.76 W/m^2/μm/sr for the tropical profile, -0.38 W/m^2/μm/sr for the mid-latitude profile, -0.11 W/m^2/μm/sr for the polar profile and -0.16 W/m^2/μm/sr for the overall cases) is less than that of another channel (1.71 W/m^2/μm/sr for the tropical profile, 0.61 W/m^2/μm/sr for the mid-latitude profile, 0.20 W/m^2/μm/sr for the polar profile and 0.43 W/m^2/μm/sr for the overall cases). In summary, the TOA radiance of the Landsat-7 TIR channel can be accurately decomposed into that of two virtual MODIS TIR channels using the empirical linear regression model

$$\begin{cases} L_{\text{MODIS}-31v} = k_1 \cdot L_{\text{Landsat7}-\text{TIR}} + b_1 \\ L_{\text{MODIS}-32v} = k_2 \cdot L_{\text{Landsat7}-\text{TIR}} + b_2 \end{cases} \tag{3}$$

where $L_{\text{MODIS-31}\,v}$, $L_{\text{MODIS-32}\,v}$, and $L_{\text{Landsat7-TIR}}$ are the TOA radiance of two virtual MODIS TIR channels and the Landsat-7 TIR channel. The linear regression coefficients k_i, b_i can be obtained by fitting from the spatially matched, adjacent time observed Landsat-7 and MODIS L1 level TOA thermal radiance remote sensing images using the random sample consensus algorithm [26], which can reduce the influences of outliers.

C. TCD-SW Algorithm

After obtaining two virtual MODIS TIR channels, the TCD-SW algorithm was developed based on the generalized nonlinear SW algorithm for producing MODIS LST products [11]

$$T_S = a_0 + \left(a_1 + a_2\frac{1-\overline{\varepsilon}}{\overline{\varepsilon}} + a_3\frac{\Delta\varepsilon}{\overline{\varepsilon}^2}\right)\left(\frac{T_i+T_j}{2}\right) + \left(a_4 + a_5\frac{1-\overline{\varepsilon}}{\overline{\varepsilon}} + a_6\frac{\Delta\varepsilon}{\overline{\varepsilon}^2}\right)\left(\frac{T_i-T_j}{2}\right) + a_7(T_i-T_j)^2 \tag{4}$$

TABLE I
TCD-SW ALGORITHM COEFFICIENTS AND RMSES IN DIFFERENT CWV INTERVALS

CWV (g/cm^2)	a_0	a_1	a_2	a_3	a_4	a_5	a_6	a_7	RMSE (K)
[0.0, 3.0)	4.048	0.993	0.132	-0.022	6.435	0.130	0.484	0.648	0.93
[3.0, 6.3]	-25.650	1.087	0.062	-0.013	9.577	7.731	-0.752	0.055	1.39
[0.0, 6.3]	8.856	0.976	0.121	-0.021	8.176	-7.260	1.544	0.196	1.26

where $\bar{\varepsilon}$ is the averaged emissivity and $\triangle\varepsilon$ is the channel emissivity difference. T_i and T_j are the TOA *BT*s in two virtual MODIS TIR channels, a_k ($k = 0, 1, \ldots, 7$) denotes the SW algorithm coefficients that can be fitted using the simulation dataset constructed above.

Since the accuracy of the SW algorithm is greatly affected by the CWV, the coefficients were often to be fitted separately in different CWV intervals in the previous studies to ensure the LST retrieval performance [9], [27]. Besides, the studies of the SC algorithm showed that there is an obvious increase in the LST error when the CWV exceeds 3.0 g/cm^2 since the assumptions are not valid in the humid atmosphere [3], [6]. Therefore, the TCD-SW algorithm was constructed in three CWV intervals ([0.0, 3.0), [3.0, 6.3], and [0.0, 6.3] g/cm^2) and compared with the SC algorithm separately to illustrate the effectiveness of the proposed method in various circumstances. Since the field of view of the Landsat-7 ETM+ sensor is about 15° from 705 km orbit, the angular effect of LST is not obvious [28], [29] and its resulting error can be neglected. Therefore, the angle correction is not considered in the proposed TCD-SW algorithm.

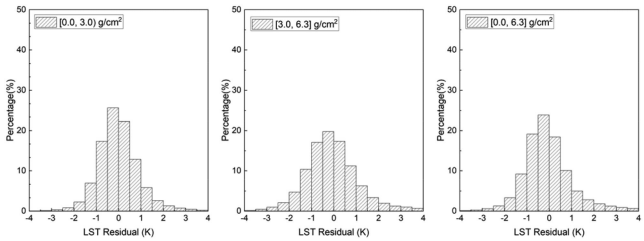

(a) (b) (c)

Fig. 4. Histograms of LST residuals of the TCD-SW algorithm.

TABLE II
COMPARISON OF LST RETRIEVAL RESULTS

CWV (g/cm^2)	SC (K)	TCD-SW (K)	$\triangle$RMSE (K)
[0.0, 3.0)	1.22	0.93	0.29
[3.0, 6.3]	2.96	1.39	1.57
[0.0, 6.3]	1.50	1.26	0.24

III. EXPERIMENTAL RESULTS

A. TCD-SW Algorithm Results

The TCD-SW algorithm was developed for different CWV intervals based on the simulation dataset, and of the 946 atmospheric profiles used, 846 profiles for CWV within [0.0, 3.0) g/cm^2, and the other 100 profiles for CWV within [3.0, 6.3] g/cm^2. Besides, there are multiple noises in practice, including the channel emissivity errors and the noise equivalent differential temperature (NE$\triangle$T) of both Landsat-7 and MODIS TIR sensors, that will affect the performance of the proposed algorithm when applied to the real remote sensing images. Therefore, multiple types of noise, including NE$\triangle$T with 0.21 K to the BT of the Landsat-7 TIR channel [30], NE$\triangle$T with 0.05 K to the BTs of the MODIS 31 and 32 channels [31], and 0.015 uncertainty of channel emissivity [29] of all channels, were added to the simulation dataset to better represent real satellite observations.

The algorithm coefficients of (4) were obtained by the multiple linear regression method and given in Table I, the used BTs of the two virtual TIR channels were fitted by the Landsat-7 and MODIS 31 and 32 data with noise in the simulation dataset. The results suggest that the RMSE increases from 0.93 to 1.39 K as the CWV grows, and the RMSE in the overall CWV interval is 1.26 K. The histogram of the LST retrieval error distribution is shown in Fig. 4, for each CWV interval, most of the LST errors are within [−1.0, 1.0] K, accounting for 78.08% for CWV $\in$ [0.0, 3.0) g/cm^2, 65.38% for CWV $\in$ [3.0, 6.3] g/cm^2, and 71.44% for CWV $\in$ [0.0, 6.3] g/cm^2, respectively. Therefore, the proposed TCD-SW algorithm using the virtual TIR channels decomposed from the Landsat-7 TIR channel can obtain accurate theoretical LST retrieval results.

B. Comparison With the SC Algorithm

To further illustrate the effectiveness of the TCD-SW algorithm, this article compares its retrieval accuracy with that of the SC algorithm in different water vapor intervals, and the RTE-based SC algorithm was selected in this article, which achieved better performance compared with other algorithms [13]. Since the SC algorithm requires known atmospheric parameters and could introduce more errors due to the uncertainty of atmospheric profiles when applied practically, therefore, 10% CWV noise and 1 K air temperature variation of each layer were added to the TIGR atmospheric profiles according to the previous study [32], and the profiles including errors were integrated into the MODTRAN model for parameter acquisition and atmospheric correction. The comparison results are given in Table II and the histograms of LST residuals of the SC algorithm are shown in Fig. 5, it can be seen that the accuracy of the SC algorithm also decreases when the CWV content rises. When the CWV is lower than 3.0 g/cm^2, the RMSE is 1.22 K with 55.35% residuals at [−1.0, 1.0] K, which is 0.29 K higher than the proposed TCD-SW algorithm, and the error increment increases substantially to 1.59 K when the water vapor content is higher than 3.0 g/cm^2 with RMSE = 2.98 K and 38.30% residuals at [−1.0, 1.0] K. In the overall CWV interval, the RMSE of the SC algorithm is 1.50 K with 53.54% residuals at [−1.0, 1.0] K and the results of the

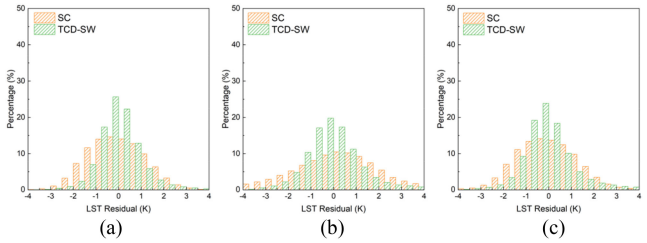

Fig. 5. Comparison of LST residual histograms of the two algorithms. (a) [0.0, 3.0) g/cm^2 . (b) [3.0, 6.3] g/cm^2. (c) [0.0, 6.3] g/cm^2.

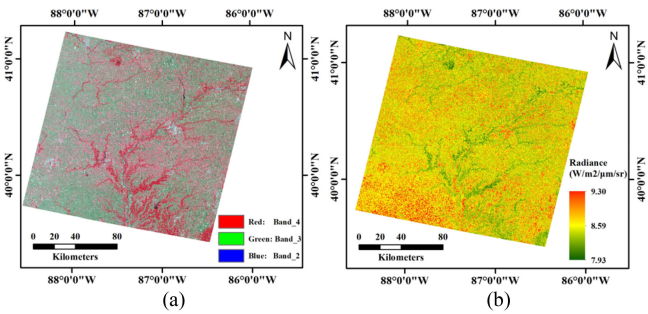

Fig. 6. Sample Landsat 7 image. (a) False color. (b) TOA radiance.

proposed TCD-SW algorithm has an accuracy improvement of 0.24 K. The residuals of both algorithms showed considerable increases when the CWV is more than 3.0 g/cm^2, and the SC algorithm occurred with obviously more residuals with errors greater than 2.5 K, which showed higher dispersion for higher CWV values as previous study [6]. By introducing the MODIS TIR channel information, the error of the proposed TCD-SW algorithm including the channel decomposition noise is smaller than that of the SC algorithm with atmospheric uncertainty, thus obtaining more accurate LST results, especially under humid atmospheric conditions, which shows that the assumption of this article is valid.

IV. Application and Validation

The TCD-SW algorithm was used to retrieve LST from multiple Landsat-7 TIR remote sensing images covering a variety of land cover types including cropland, grassland, and ocean from 2002 to 2019 for multiple regions worldwide, and the results were compared with the corresponding Landsat-7 products based on the ground measurement data and well-validated MODIS products.

A. Landsat-7 LST Retrieval

1) Channel Decomposition Regression: The TOA radiance of the Landsat-7 TIR channel was decomposed by combining the MODIS 31 and 32 channels data, and the linear regression coefficients in Section II-B were calculated based on the homogeneous pixels after resampling and matching using the data processing method presented in the previous study [16]. The Landsat-7 data acquired on September 23, 2002, with the Path/Row number of

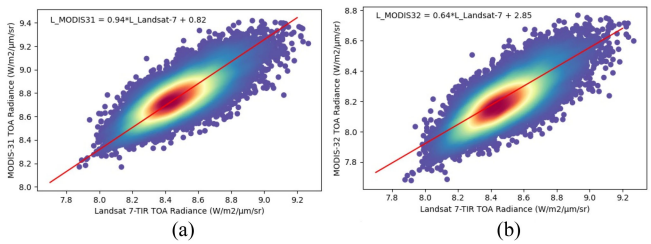

Fig. 7. Example of TOA radiance linear regression results. (a) MODIS 31 channel.(b) MODIS 32 channel.

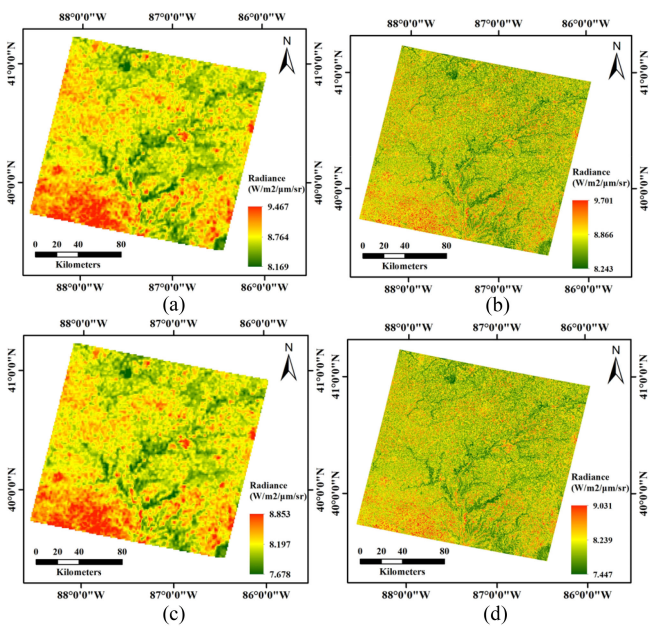

Fig. 8. Comparison of original and decomposed TIR TOA radiance. (a) Original MODIS 31 channel. (b) Decomposed MODIS 31 channel. (c) Original MODIS 32 channel. (d) Decomposed MODIS 32 channel.

022/032 was selected as the example image (see Fig. 6). The spatial extent of the sample image is located on the border between Illinois and Indiana, USA, and the latitude and longitude of the upper left corner are 41.29721°N and 88.73307°W. The most abundant land surface type within the sample image is cropland, but most of it has little crop cover and may be harvested or unplanted. This is followed by forest, which is mainly located in the middle of the south, interspersed with cropland and with dense vegetation cover. In addition, some impervious surfaces are scattered in the image, mainly urban and roads, etc. The results of linear regression and band decomposition of TOA radiance after its matching with the MOD021KM product from adjacent time observations are shown in Figs. 7 and 8 (clipped by the Landsat Path Row Shapefile), respectively. It can be seen that there is a good correlation between the TOA radiance of different sensors despite the presence of a few outliers for the real TIR remote sensing image pairs, and the decomposed TOA radiance images maintain the same spatial distribution and similar data range as the real MODIS data. For the sample image, there is a high-temperature aggregates zone in the southwest corner, with

some high-temperature spots scattered in other locations, and low-temperature forested pixels distributed in the middle. For the TOA radiance, similar to the results in the simulation dataset, the range of values in the Landsat 7 image lies between that of the MODIS 31 and 32 channels images. The decomposed MODIS TIR images present richer image details, for example, the decomposition results present differences in land surface thermal radiance under different vegetation cover conditions within the high-temperature aggregation zone, rather than the high radiance values in almost all pixels before decomposition in Fig. 8.

2) Land Surface Emissivity Derivation: The SW algorithm requires that the LSE is known, and the classification-based emissivity method [29] was used in this article. Assuming that the pixels are formed by vegetation and background components, and the emissivity of each component for different land cover types is the empirical value given by the spectral library [21], [22]. For a given land cover type, there are three categories: soil, mixed, and vegetation, depending on the normalized difference vegetation index (NDVI) value which is obtained using the land surface reflectance of Landsat-7 red and near-infrared channel, the pixel emissivity ε of the virtual MODIS TIR channels is calculated as follows [33]:

$$\begin{array}{ll} \mathrm{NDVI} < \mathrm{NDVI}_s & \varepsilon = c + \sum a_\lambda \cdot \rho_\lambda \\ \mathrm{NDVI} \geq \mathrm{NDVI}_v & \varepsilon = \varepsilon_v + d\varepsilon \\ \mathrm{NDVI}_s \leq \mathrm{NDVI} \leq \mathrm{NDVI}_v & \varepsilon = \varepsilon_v \cdot f + \varepsilon_g \cdot (1-f) \\ & \quad + 4 \cdot d\varepsilon \cdot f \cdot (1-f) \end{array} \tag{5}$$

where NDVI_s and NDVI_v are the NDVI threshold for barren soil and fully vegetated pixel, which was set as 0.20 and 0.86 [27] in this article, separately. ρ_λ is the channel reflectance of the optical reflective channel, a_λ and c are the coefficients, ε_v and ε_g are the emissivities of the vegetation and background component, and $d\varepsilon$ is the emissivity increment caused by the cavity effect of multiple scattering within the pixel [34]. For the mixed pixel, the component ratio is represented by the fraction vegetation cover f, which can be calculated as [35]

$$f = \left(\frac{\mathrm{NDVI} - \mathrm{NDVI}_s}{\mathrm{NDVI}_v - \mathrm{NDVI}_s} \right)^2. \tag{6}$$

3) Atmospheric Water Vapor Estimation: In addition to the LSE, the CWV determines which set of TCD-SW algorithm coefficients in Table I is used, estimated by the modified SW covariance-variance ratio method [36] in this article, and can be expressed as

$$\mathrm{CWV} = a \cdot (\tau_\mathrm{j}/\tau_\mathrm{i})^2 + b \cdot \tau_\mathrm{j}/\tau_\mathrm{i} + c \tag{7}$$

$$\begin{aligned} \tau_j/\tau_i &= (\varepsilon_i/\varepsilon_j) \cdot R_{ji} \approx R_{ji} \\ &= \sum_{k=1}^{N} \left(T_{i,k} - \bar{T}_i\right)\left(T_{j,k} - \bar{T}_j\right) \Big/ \sum_{k=1}^{N} \left(T_{i,k} - \bar{T}_i\right)^2 \end{aligned} \tag{8}$$

where i and j represent the two MODIS TIR channels, τ is the channel atmospheric transmittance, ε is the emissivity, N is the number of adjacent clear sky pixels, $T_{i,k,}$ and $T_{j,k}$ are the pixel BTs of channel i and j, $\bar{T}$ is the mean BTs of the adjacent N pixels.

TABLE III
INFORMATION ON GROUND VALIDATION SITES

Name	Land Cover	Location
PKULSTNet-HBC	Grassland	42.41°N / 117.25°E
PKULSTNet-CQB	Orchard	29.76°N / 106.32°E
PKULSTNet-HNT	Grassland	19.68°N / 111.02°E
PKULSTNet-XJF	Grassland	44.38°N / 87.92°E
SURFRAD-FPK	Grassland	48.31°N / 105.10°W
SURFRAD-SXF	Cropland	43.73°N / 96.62°W
SURFRAD-PSU	Cropland	40.72°N / 77.93°W
SURFRAD-BND	Cropland	40.05°N / 88.37°W
SURFRAD-DRA	Rock	36.62°N / 116.02°W
SURFRAD-GWN	Pasture	34.25°N / 89.87°W

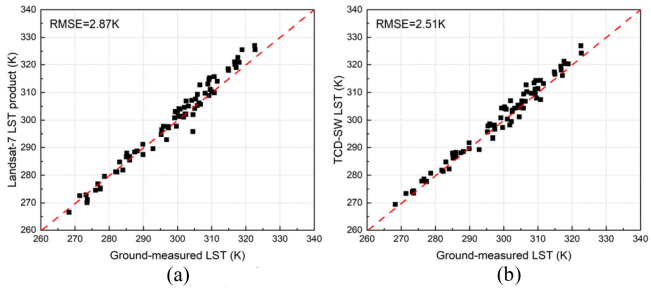

Fig. 9. Validation results using ground site data. (a) Landsat-7 LST products. (b) TCD-SW algorithm results.

The approximation that $\tau_j/\tau_i \approx R_{ji}$ by considering the emissivity ratio $\varepsilon_i/\varepsilon_j$ equal to 1, which is acceptable for the most land surfaces [36].

B. Results Validation

1) Validation Using the Site-Measured Data: A total of 77 Landsat-7 images from 2002 and 2019 were collected at the surface radiation budget network (SURFRAD) [37] and the Peking University LST network (PKULSTNet) [27] data, the information on ground validation sites which are located in several regions of China and the United States and contain different land cover types such as grassland, cropland, and rock is given in Table III. The ground measured data was processed by the method based on Stefan–Boltzmann law [38], and the Landsat-7 LST product and the results of the TCD-SW algorithm are both compared with the ground measurement LST data, the validation results are shown in Fig. 9. It can be seen that the TCD-SW algorithm achieves more accurate results with an RMSE of 2.51 K, which is 0.36K smaller than the RMSE of the Landsat-7 LST product, and the advantage of not relying on known atmospheric parameters reduces the effect of its uncertainty in the SC algorithm.

Most of the above remote sensing images used for validation using ground site data have a low atmospheric water vapor content at the time of observation, with the average CWV value below 2.0 g/cm^2. As shown in the previous analysis, the theoretical advantage of the TCD-SW algorithm is more obvious in a humid atmosphere, especially when the CWV is greater than 3.0 g/cm^2. To further illustrate the effectiveness of the method in

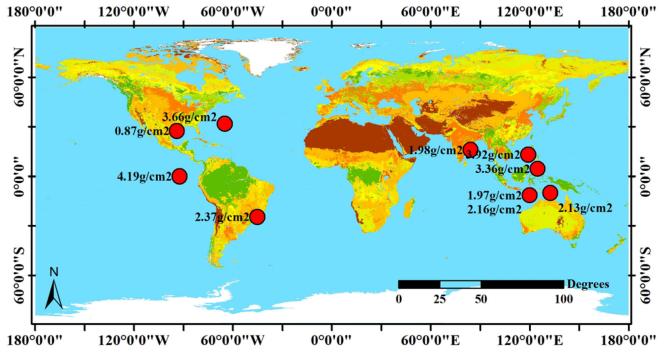

Fig. 10. Location of Landsat-7 remote sensing images used to validate SST with corresponding CWV values (the background image came from the MODIS global land cover types in 2002, with a spatial resolution of 0.05°).

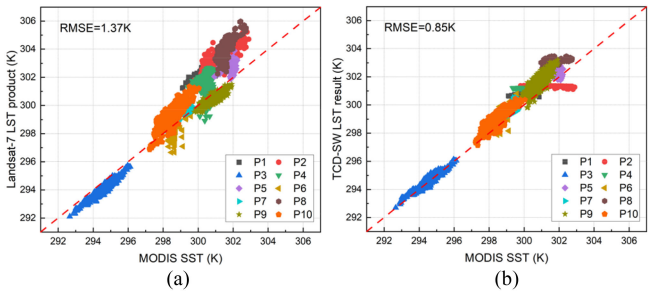

Fig. 11. Cross- comparison results using MODIS SST products. (a) Landsat-7 LST products. (b) TCD-SW algorithm results.

this article, the subsurface of the ocean, where the atmosphere is more humid, is also selected as the validation area.

2) Cross-Comparison With the MODIS SST Product: The previous study [39] showed that the MODIS sea surface temperature (SST) product has proven to be an adequate source of ground truth after the comparison with the buoy data, which has been applied for the global validation of the Landsat-7 LST product. Therefore, ten Landsat-7 images from different ocean regions are chosen (see Fig. 10), there are four images with CWV greater than 3.0 g/cm^2, and seven images with CWV greater than 2.0 g/cm^2, and the average CWV is 2.7 g/cm^2. The LST products and the LST estimation results of the proposed TCD-SW algorithm are cross-compared with the MODIS SST product according to the method of matching local homogeneity pixels [39]. A total of 3162 sets of matched data pairs were obtained, and the SST validation results are shown in Fig. 11. Compared with the MODIS SST product, the accuracy of both algorithms for SST estimation is higher than that for LST due to the homogeneity of the ocean surface and the stability of the emissivity, but the TCD-SW algorithm results are closer to the MODIS SST product with an overall RMSE of 0.85 K and a distribution nearer to the 1:1 line. For the case of the more humid atmosphere, the RMSEs of Landsat-7 LST product and TCD-SW results are 1.69 K and 0.96 K when CWV $>$ 2.0 g/cm^2, while the RMSEs of Landsat-7 LST product and TCD-SW results are 2.18 and 1.21 K when CWV $>$ 3.0 g/cm^2. The errors of the TCD-SW algorithm results are less by 0.73 and 0.97 K, respectively, which also confirms the theoretical analysis of the conclusion that the advantages of the proposed algorithm are more obvious under humid atmospheric conditions.

V. Conclusion and Discussions

The SC algorithm is currently the only effective approach to retrieve LST from remote sensing data with one TIR channel, but its performance is highly dependent on the accuracy of the atmospheric correction which is often difficult to guarantee in the absence of simultaneously measured profiles, and the accuracy may decrease rapidly under the humid atmospheric condition. In comparison, the SW algorithm does not require known atmospheric parameters and its results are more insensitive to variations in atmospheric conditions, which can compensate for the shortcomings of the SC algorithm. However, a minimum of two TIR channels is required, making it unable to be used directly for remote sensing data with one TIR channel. According to the previous studies, there is a strong linear correlation between the observed TOA radiance of two different TIR channels with similar wavelength ranges, which makes it theoretically possible to decompose a single TIR channel into two TIR channels with small errors for close wavelengths. Therefore, this article assumes that the SW algorithm error due to the TIR channel decomposition noise is smaller than the SC algorithm error due to the atmospheric parameter uncertainty, and the TCD-SW algorithm was proposed based on the generalized nonlinear SW algorithm using two virtual TIR channels that decomposed from one Landsat-7 ETM+ TIR channel by fusion with MODIS data.

The LST retrieval results obtained from the simulation dataset including emissivity error, NE$\triangle$T noise showed that the TCD-SW algorithm has good theoretical performance, the RMSEs are below 1.5 K in all CWV intervals. In contrast, the TCD-SW algorithm achieved more accurate results in every CWV interval, especially when the CWV exceeds 3.0 g/cm^2, and the RMSE was decreased by 1.57 K using the proposed algorithm. And the error improves by more than 0.2 K both when the CWV is less than 3 g/cm^2, and in the overall CWV interval. As for the sensitivity to atmospheric changes, the RMSE of the TCD-SW algorithm grows only 0.46 K when the CWV increased, while the SC algorithm grows 1.74 K. It can be seen that the TCD-SW algorithm fusing multisource data, although it may introduce some noise due to fitting errors, still has the advantage of being insensitive to atmospheric uncertainty compared to the SC algorithm, especially in humid atmospheres, which can theoretically effectively improve the LST retrieval accuracy. Ground validation using the SURFRAD and the PKULSTNet site measured data was carried out based on Landsat-7 remote sensing images from 2002 and 2019, respectively. The results of the TCD-SW algorithm and the Landsat-7 L2-level LST products were compared for croplands, grasslands, and forests in China and the USA of different seasons, respectively, and the TCD-SW algorithm achieved more accurate results. In addition, the results of the LST validation conducted based on the MODIS SST product also indicated that the accuracy improvement of the TCD-SW algorithm over the SC algorithm under humid

atmospheric conditions grows as the CWV increases. This indicates that in the practical application, the MODIS 31 and 32 TIR channels from simultaneous observations are suitable for channel decomposition of Landsat-7 TOA radiance, which helps to improve the LST retrieval accuracy in complicated atmospheric situations.

Although this article demonstrates the validity of the proposed TCD-SW algorithm using both the simulation dataset and ground measured data, However, there are some limitations to the use of the algorithm, and some further studies are needed in future work. First, the use of the TCD-SW algorithm presupposes that there are enough valid pixels to match and fit to obtain the coefficients of the channel decomposition model. Therefore, too much cloud coverage or image noise may make the TCD-SW algorithm inaccurate or even unusable. Therefore, the applicability of the TCD-SW algorithm will be expected to be improved by establishing a global atmospheric background and forming a look-up table for the channel decomposition algorithm coefficients under different observation conditions to reduce the reliance on simultaneous multisource data. Second, although the transit times of Landsat-7 and Terra are close, c changes in land surface thermal radiance may still occur due to weather changes, clouds, and other factors. Therefore, to improve the performance of the TCD-SW algorithm, it is necessary to carry out the time normalization method [40], [41] to weaken the effect of satellite transit time differences. Third, the spatial resolution of the images from the two TIR data sources varies greatly. In this article, the resolution of the Landsat-7 image was reduced to 1 km to match the MODIS image. However, this loses the detailed information in the high-resolution images, especially in complex surface conditions such as urban and mountainous areas. The development of a new downscaling method considering multifactor and geographical weights is expected to further increase the accuracy. In addition, the TIR channel decomposition model in this article is linear, and although it presents a good correlation in the simulation dataset, many outliers appear when used for real TIR remote sensing images. Therefore, nonlinear machine learning models that consider more parameters, such as BT range, land cover types, and air temperature with stronger robustness can also be developed to optimize the TCD-SW algorithm. Finally, the TCD-SW algorithm in this article is proposed based on the empirical statistical law between the TOA radiance in the TIR channel of different remote sensing data sources with similar wavelength ranges, the physical theoretical basis of TIR channel decomposition requires further in-depth analysis, including finding the wavelength ranges and BTs that are suitable for decomposition, as well as the quantitative description of the errors that may result from changes in wavelengths and SRF before and after the channel decomposition.

Acknowledgment

The authors would like to thank the computing resource provided by the high-performance computing platform of Peking University.

References

[1] L. M. McMillin, "Estimation of sea surface temperatures from two infrared window measurements with different absorption," *J. Geophys. Res.*, vol. 80, no. 36, pp. 5113–5117, 1975.

[2] Z.-L. Li *et al.*, "Satellite-derived land surface temperature: Current status and perspectives," *Remote Sens. Environ.*, vol. 131, pp. 14–37, 2013.

[3] J. C. Jimenez-Munoz, J. Cristobal, J. A. Sobrino, G. Soria, M. Ninyerola, and X. Pons, "Revision of the single-channel algorithm for land surface temperature retrieval from landsat thermal-infrared data," *IEEE Trans. Geosci. Remote Sens.*, vol. 47, no. 1, pp. 339–349, Jan. 2009, doi: 10.1109/tgrs.2008.2007125.

[4] J. C. Jiménez-Muñoz and J. A. Sobrino, "A generalized single-channel method for retrieving land surface temperature from remote sensing data," *J. Geophys. Res. Atmos.*, vol. 108, 2003.

[5] Z. Qin, A. Karnieli, and P. Berliner, "A mono-window algorithm for retrieving land surface temperature from landsat TM data and its application to the Israel-Egypt border region," *Int. J. Remote Sens.*, vol. 22, no. 18, pp. 3719–3746, 2001.

[6] J. Cristóbal, J. Jiménez-Muñoz, A. Prakash, C. Mattar, D. Skoković, and J. Sobrino, "An improved single-channel method to retrieve land surface temperature from the landsat-8 thermal band," *Remote Sens.,* vol. 10, no. 3, 2018, Art. no. 431.

[7] F. Becker and Z.-L. Li, "Towards a local split window method over land surfaces," *Int. J. Remote Sens.*, vol. 11, no. 3, pp. 369–393, 1990.

[8] C. Du, H. Ren, Q. Qin, J. Meng, and S. Zhao, "A practical split-window algorithm for estimating land surface temperature from landsat 8 data," *Remote Sens.,* vol. 7, no. 1, pp. 647–665, 2015.

[9] X. Ye, H. Ren, R. Liu, Q. Qin, Y. Liu, and J. Dong, "Land surface temperature estimate from chinese gaofen-5 satellite data using split-window algorithm," *IEEE Trans. Geosci. Remote Sens.*, vol. 55, no. 10, pp. 5877–5888, Oct. 2017, doi: 10.1109/tgrs.2017.2716401.

[10] Y. Chen, S.-B. Duan, J. Labed, and Z.-L. Li, "Development of a split-window algorithm for estimating sea surface temperature from the chinese gaofen-5 data," *Int. J. Remote Sens.*, vol. 40, no. 5-6, pp. 1621–1639, 2018.

[11] Z. Wan, "New refinements and validation of the collection-6 MODIS land-surface temperature/emissivity product," *Remote Sens. Environ.*, vol. 140, pp. 36–45, 2014.

[12] B. Tang, "Nonlinear split-window algorithms for estimating land and sea surface temperatures from simulated chinese gaofen-5 satellite data," *IEEE Trans. Geosci. Remote Sens.*, vol. 56, no. 11, pp. 6280–6289, Nov. 2018, doi: 10.1109/tgrs.2018.2833859.

[13] X. Yu, X. Guo, and Z. Wu, "Land surface temperature retrieval from landsat 8 TIRS—Comparison between radiative transfer equation-based method, split window algorithm and single channel method," *Remote Sens.*, vol. 6, no. 10, pp. 9829–9852, 2014.

[14] V. García-Santos, J. Cuxart, D. Martínez-Villagrasa, M. Jiménez, and G. Simó, "Comparison of three methods for estimating land surface temperature from landsat 8-TIRS sensor data," *Remote Sens.*, vol. 10, no. 9, 2018, Art. no. 1450.

[15] D. Sun and R. T. Pinker, "Estimation of land surface temperature from a geostationary operational environmental satellite (GOES-8)," *J. Geophys. Res.*, vol. 108, no. D11, 2003.

[16] X. Ye *et al.*, "Cross-calibration of chinese gaofen-5 thermal infrared images and its improvement on land surface temperature retrieval," *Int. J. Appl. Earth Observ. Geoinf.*, vol. 101, 2021, Art. no. 102357.

[17] Y. Chen, S.-B. Duan, H. Ren, J. Labed, and Z.-L. Li, "Algorithm development for land surface temperature retrieval: Application to chinese gaofen-5 data," *Remote Sens.*, vol. 9, no. 2, 2017, Art. no. 161.

[18] X. Meng and J. Cheng, "Estimating land and sea surface temperature from cross-calibrated chinese gaofen-5 thermal infrared data using split-window algorithm," *IEEE Geosci. Remote Sens. Lett.*, vol. 17, no. 3, pp. 509–513, Mar. 2020, doi: 10.1109/lgrs.2019.2921863.

[19] Q. Weng, P. Fu, and F. Gao, "Generating daily land surface temperature at landsat resolution by fusing landsat and MODIS data," *Remote Sens. Environ.*, vol. 145, pp. 55–67, 2014.

[20] F. Chevallier, F. Chéruy, N. A. Scott, and A. Chédin, "A neural network approach for a fast and accurate computation of a longwave radiative budget," *J. Appl. Meteorol.*, vol. 37, no. 11, pp. 1385–1397, 1998,.

[21] C. S. William, Z. Wan, Y. Zhang, and Y. Feng, "Thermal infrared (3–14 μm) bidirectional reflectance measurements of sands and soils," *Remote Sens. Environ.*, vol. 60, no. 1, pp. 101–109, 1997.

[22] A. M. Baldridge, S. J. Hook, C. I. Grove, and G. Rivera, "The ASTER spectral library version 2.0," *Remote Sens. Environ.*, vol. 113, no. 4, pp. 711–715, 2009.

[23] Z. Wan and J. Dozier, "A generalized split-window algorithm for retrieving land-surface temperature from space," *IEEE Trans. Geosci. Remote Sens.*, vol. 34, no. 4, pp. 892–905, Jul. 1996.

[24] Z. Wan, "New refinements and validation of the MODIS land-surface temperature/emissivity products," *Remote Sens. Environ.*, vol. 112, no. 1, pp. 59–74, 2008.

[25] Z. Wan and Z. L. Li, "Radiance-based validation of the V5 MODIS land-surface temperature product," *Int. J. Remote Sens.*, vol. 29, no. 17-18, pp. 5373–5395, 2010.

[26] M. A. Fischler and R. C. Bolles, "Random sample consensus: A paradigm forModelFitting with applications to image analysis and automated cartography," *Commun. ACM*, vol. 24, no. 6, pp. 381–395, 1981.

[27] Y. Zheng *et al.*, "Land surface temperature retrieval from Sentinel-3A sea and land surface temperature radiometer, using a split-window algorithm," *Remote Sens.*, vol. 11, no. 6, 2019, Art. no. 650.

[28] H. Ren *et al.*, "Performance evaluation of four directional emissivity analytical models with thermal SAIL model and airborne images," *Opt. Exp.*, vol. 23, no. 7, pp. A346–A360, Apr. 2015.

[29] Z.-L. Li *et al.*, "Land surface emissivity retrieval from satellite data," *Int. J. Remote Sens.*, vol. 34, no. 9/10, pp. 3084–3127, 2013.

[30] T. Arvidson, J. Barsi, M. Jhabvala, and D. Reuter, *Landsat and Thermal Infrared Imaging (Thermal Infrared Remote Sensing)*. Dordrecht, The Netherlands: Springer, 2013.

[31] S. Madhavan *et al.*, "Noise characterization and performance of MODIS thermal emissive bands," *IEEE Trans. Geosci. Remote Sens.*, vol. 54, no. 6, pp. 3221–3234, Jun. 2016, doi: 10.1109/TGRS.2015.2514061.

[32] C. Coll, V. Caselles, E. Valor, and R. Niclòs, "Comparison between different sources of atmospheric profiles for land surface temperature retrieval from single channel thermal infrared data," *Remote Sens. Environ.*, vol. 117, pp. 199–210, 2012.

[33] H. Ren, R. Liu, Q. Qin, W. Fan, L. Yu, and C. Du, "Mapping finer-resolution land surface emissivity using landsat images in China," *J. Geophys. Res. Atmos.*, vol. 122, no. 13, pp. 6764–6781, 2017.

[34] E. Caselles, E. Valor, F. Abad, and V. Caselles, "Automatic classification-based generation of thermal infrared land surface emissivity maps using AATSR data over europe," *Remote Sens. Environ.*, vol. 124, pp. 321–333, 2012.

[35] B.-H. Tang, K. Shao, Z.-L. Li, H. Wu, and R. Tang, "An improved NDVI-based threshold method for estimating land surface emissivity using MODIS satellite data," *Int. J. Remote Sens.*, vol. 36, no. 19-20, pp. 4864–4878, 2015.

[36] H. Ren *et al.*, "Atmospheric water vapor retrieval from landsat 8 thermal infrared images," *J. Geophys. Res. Atmos.*, vol. 120, no. 5, pp. 1723–1738, 2015.

[37] J. A. Augustine, G. B. Hodges, C. R. Cornwall, J. J. Michalsky, and C. I. Medina, "An update on SURFRAD—The GCOS surface radiation budget network for the continental United States," *J. Atmos. Ocean. Technol.*, vol. 22, pp. 1460–1472, 2005.

[38] H. Zeng, H. Ren, J. Nie, J. Zhu, X. Ye, and C. Jiang, "Land surface temperature and emissivity retrieval from nighttime middle and thermal infrared images of chinese Fengyun-3D MERSI-II," *IEEE J. Sel. Top. Appl. Earth Obs. Remote Sens.*, vol. 14, pp. 7724–7733, 2021, doi: 10.1109/jstars.2021.3098579.

[39] K. G. Laraby and J. R. Schott, "Uncertainty estimation method and landsat 7 global validation for the landsat surface temperature product," *Remote Sens. Environ.*, vol. 216, pp. 472–481, 2018.

[40] S.-B. Duan, Z.-L. Li, B.-H. Tang, H. Wu, and R. Tang, "Generation of a time-consistent land surface temperature product from MODIS data," *Remote Sens. Environ.*, vol. 140, pp. 339–349, 2014.

[41] W. Zhao, H. Wu, G. Yin, and S.-B. Duan, "Normalization of the temporal effect on the MODIS land surface temperature product using random forest regression," *ISPRS J. Photogramm. Remote Sens.*, vol. 152, pp. 109–118, 2019.

Xin Ye received the B.S. degree from Beijing Normal University, Beijing, China, in 2012; and the Ph.D. degree from Peking University, Beijing, China, in 2017.

He is currently a Postdoctoral Researcher with the Institute of Remote Sensing and Geographic Information System, School of Earth and Space Sciences, Peking University, Beijing, China. His research mainly concentrates on thermal infrared remote sensing and deep learning.

Huazhong Ren received the Ph.D. degree from Beijing Normal University, China and from the Université de Strasbourg, Strasbourg, France in 2013.

He is currently an Associate Professor with Tenure in the Institute of Remote Sensing and Geographic Information System, School of Earth and Space Sciences, Peking University, Beijing, China. His research interests include land surface temperature/emissivity estimate from thermal infrared remote sensing data.

Jinshun Zhu received the B.S. degree, in 2019, from Peking University, Beijing, China, where he is currently working toward the Ph.D. degree with the Institute of Remote Sensing and Geographic Information System, School of Earth and Space Sciences, Peking University, Beijing, China.

His research interests mainly concentrate on middle infrared and thermal infrared remote sensing.

Hui Zeng received the B.S. degree in geographic information system from Lanzhou Jiaotong University, Lanzhou, China, in 2011. He is currently working toward the Master's degree with the Institute of Remote Sensing and Geographic Information System, School of Earth and Space Sciences, Peking University, Beijing, China.

His main research interests include land surface temperature and emissivity estimate from the thermal infrared image.

Baozhen Wang received the B.S. degree in cartography and geography information system from Information Engineering University, Zhengzhou, China, in 2017. He is currently working toward the master's degree with the Institute of Remote and Geographic Information System, School of Earth and Space Sciences, Peking University, Beijing, China.

His main research interests include sea surface temperature and emissivity estimate from the thermal infrared image.

He Huang received the master's degree from Beijing Normal University, Beijing, China in 2011.

Since 2011, she has been a Senior Engineer with Chongqing Planning Exhibition Gallery, Chongqing, China (Chongqing Planning Research Institute). Her research interests include urbanization and urban planning.

Wenjie Fan received the Ph.D. degree in physical geography from the College of Urban and Environmental Sciences, Peking University (PKU), Beijing, China, in 2000.

She has completed the Post doctorate Research with the Institute of Remote Sensing and GIS (IRSGIS), PKU, in 2002. She is currently a Professor with the IRSGIS, PKU. She has continued to work on and manage research projects on vegetation remote sensing, scale effects of remote sensing, hyperspectral remote sensing, and application of remote sensing in ecology and environment management for years. She has authored or coauthored more than 90 papers, including 40 papers indexed by SCI. She has also been the PI of more than seven National Natural funds and other research projects.